Nonlinear Reduced-Order Models for Thermoelastodynamic Response of Isotropic and Functionally Graded Panels

R. Perez,* X. Q. Wang,† and Marc P. Mignolet‡
Arizona State University, Tempe, Arizona 85287-6106

The focus of this investigation is on the development and validation of thermoelastic reduced-order models for the geometrically nonlinear response and temperature of heated structures. The reduced-order modeling approach is based on a modal-type expansion of both displacements and temperatures in the undeformed, unheated configuration. A set of coupled nonlinear differential equations governing the time-varying generalized coordinates of the response and temperature expansion are derived from finite thermoelasticity using a Galerkin approach. Furthermore, the selection of the basis functions to be used in these reduced-order models is discussed, and the numerical evaluation of the model coefficients is addressed. This approach is first validated on an isotropic beam subjected to both thermal effects and external loads. The thermal effects are large enough to induce a significant buckling of the panel, while the time-varying loads lead to snap-throughs ranging in frequency from infrequent to continuous. Validation to a functionally graded material panel in similar conditions is then performed. In both cases, the reduced-order modeling predicted temperatures and responses are found to very closely match their full finite element counterparts.

Nomenclature

B = capacitance matrix, physical coordinates
b^0 = body force vector with respect to the undeformed configuration, physical coordinates
C = fourth-order elasticity tensor, physical coordinates
C_v = specific heat per unit mass measured in the state of constant strain
D = damping matrix, modal coordinates
E = Green strain tensor, physical coordinates
$\mathcal{E}$ = elastic energy
F = deformation gradient tensor, physical coordinates
$\mathcal{F}$ = Helmholtz free energy (per unit mass)
F_i = ith force from external excitation, modal coordinates
$F_i^{(\mathrm{th})}$ = force induced by thermal variation, modal coordinates
k = conductivity tensor in the deformed configuration, physical coordinates
$\tilde{K}$ = conductance matrix, modal coordinates
$K_{ijl}^{(\mathrm{th})}$ = temperature-dependant term of the linear stiffness matrix, modal coordinates
$K_{ijl}^{(2)}$ = element of the third-order tensor associated with the quadratic stiffness terms, modal coordinates
$K_{ijlp}^{(3)}$ = element of the fourth-order tensor associated with cubic stiffness terms, modal coordinates
$K^{(1)}$ = linear stiffness matrix, modal coordinates
k^0 = conductivity tensor pulled back to reference configuration, physical coordinates
M = mass matrix, modal coordinates

P = temperature source vector associated with boundary conditions, modal coordinates
q = response vector, modal coordinates
S = second Piola–Kirchhoff stress tensor, physical coordinates
$\mathcal{S}$ = specific entropy
T = temperature field, physical coordinates
t = time
T_0 = reference temperature field, physical coordinates
$T^{(m)}$ = thermal basis function
u = displacement vector, physical coordinates
$U^{(n)}$ = displacement basis function
α = Rayleigh damping coefficient, 1/s
α = second-order tensor of thermal expansion, physical coordinates
β = Rayleigh damping coefficient, s
δ_{ij} = Kronecker symbol
ρ_0 = density in the reference configuration
τ = thermal vector, modal coordinates
Ω_0 = structure domain in the undeformed configuration

I. Introduction

THERMAL considerations play a fundamental role in the design of panels of supersonic/hypersonic aircraft and proposed reentry vehicles with outside temperatures of the order of or exceeding 3000°F often considered typical [1]. The classical approach to mitigating these very large temperatures, and the material degradation and thermal stresses they would incur on a virgin metallic structure, has been to install a thermal protection system (TPS) on the metallic panel to minimize its heat transfer. More recently, it has been proposed to combine the TPS and the underlying metallic panel into a single structural component exhibiting variations of properties, most notably through the thickness but also possibly along the panel. These functionally graded material (FGM) panels would be composed of mixtures of ceramic and metallic materials exhibiting a high concentration of the ceramic/metal in areas where the temperature is largest/lowest.

The variations of material composition through the thickness and along the panel imply similar variations of the temperature, to which must be added temporal variations associated with the mission profile. In this light, it is clearly necessary to carry out both thermal

and structural analyses. However, should they be carried out in a coupled manner or can they be assumed to be uncoupled? Temperature is well known to affect the structural behavior through thermal strains and the associated stresses induced when the structural expansion/contraction is restrained. Thermal buckling is a typical potential outcome that is particularly significant from a structural perspective.

The effect of structural deformations on the temperature distribution is less obvious and has often been neglected in the past. In terms of *direct* effects, the most significant ones are the latency effect and the change of geometry for the heat conduction problem implied by the structural deformations. While typical panel deflections are of the order of its thickness, a large excitation (e.g., from acoustic origin) may induce the snap-through of either curved panels or buckled flat panels, leading to deformations that are then in the 10s/100s of panel thicknesses and may result in a noticeable change of geometry. Either way, the above snap-through deflections would certainly affect the aerodynamics, which would then likely induce changes in the heat flux. Thus, the structural deformations may be expected to, at least indirectly (through the aerodynamic), affect the temperature distribution (see [2]).

The preceding comments suggest that a coupled multiphysics, thermal and nonlinear structural, analysis capability should be developed for such problems. Finite element-based approaches are not particularly well suited for such problems. First, the coupling of the thermal and structural problems may not be an option in the desired commercial software package. More important, however, is the sheer computational effort to be carried out: the estimation of the fatigue damage incurred by a particular mission will likely require the computations over a very large number of (the small) time steps. Furthermore, the presence of a random acoustic loading would transform the problem into a random vibration one, which might necessitate the consideration of multiple time histories in a Monte Carlo setting.

Accordingly, it would be desirable to have a faster yet accurate prediction technique. Recent investigations [3–12] on the formulation and development of nonlinear structural reduced-order modeling (ROM) strategies are noteworthy in this regard. Indeed, they have demonstrated the fidelity and computational efficiency of such nonlinear reduced-order models for the prediction of the nonlinear geometric response of isothermal panels subjected to strong acoustic excitations. Furthermore, these ROMs are built upon a finite element model of the panel and are thus applicable to a broad range of panel geometries and boundary conditions. Finally, the tight coupling of these ROMs with the aerodynamics has also been demonstrated [13].

The combination of thermal effects and applied loads has also been considered [6,10,12], using a modal basis either independent of a homogenous temperature [6,12] or varying with it [10]. Again, these studies have demonstrated that ROMs can accurately match finite element predictions, even when the applied loads are large enough to induce the occurrence of snap-throughs of the panel from the neighborhood of one buckled position to the other [12].

Note that these investigations were carried out with a constant, homogenous temperature field, but time and space variations of this field are expected to also take place in practice, especially for FGM panels. In view of the preceding successes in connection with the structural dynamic response, it would be desirable to have 1) a similar ROM for the prediction of the temperature field and 2) a coupling strategy of the thermal and structural dynamic ROMs. Accordingly, the focus of the present investigation is on the formulation and first validation of such a coupled thermoelastodynamic ROM strategy. The emphasis is on both isotropic and FGM panels subjected to external excitations large enough to induce a geometrically nonlinear response.

II.   Nonlinear Reduced-Order Modeling

A ROM is defined here as a modal-like representation of the temperature T and displacement field u_i as

$$T(X, t) = \sum_{n=1}^{\mu} \tau_n(t) T^{(n)}(X) \tag{1}$$

for the temperature and

$$u_i(X, t) = \sum_{n=1}^{M} q_n(t) U_i^{(n)}(X) \tag{2}$$

for the displacement. In these equations, the functions $U_i^{(m)}$ and $T^{(m)}$ are specified functions of the position vector X in the *undeformed* configuration, chosen to satisfy the necessary boundary conditions.

To obtain a set of (nonlinear) ordinary differential equations governing the evolution of the generalized coordinates $q_n(t)$ and $\tau_n(t)$, it is first necessary to derive the governing field equations for the displacements $u_i(X, t)$ and temperature $T(X, t)$ in the *undeformed* configuration. Following [14–16], one obtains (see also [11])

$$\frac{\partial}{\partial X_k}(F_{ij} S_{jk}) + \rho_0 b_i^0 = \rho_0 \ddot{u}_i \quad \text{for } X \in \Omega_0 \tag{3}$$

where summation over repeated indices is implied. In this equation, S denotes the second Piola–Kirchhoff stress tensor, ρ_0 is the density in the reference configuration, and b^0 is the vector of body forces, all of which are assumed to depend on the coordinates X_i of the undeformed configuration in which the structure occupies the domain Ω_0. Furthermore, in Eq. (3), the deformation gradient tensor F is defined by its components F_{ij} as

$$F_{ij} = \frac{\partial x_i}{\partial X_j} = \delta_{ij} + \frac{\partial u_i}{\partial X_j} \tag{4}$$

where δ_{ij} denotes the Kronecker symbol and the displacement vector is $u = x - X$, x being the position vector in the deformed configuration.

The heat conduction equation on the domain Ω_0 can be written as

$$\rho_0 T \dot{\mathcal{S}} = \frac{\partial}{\partial X_i}\left[k_{ij}^0 \frac{\partial T}{\partial X_j}\right] \tag{5}$$

where $\mathcal{S}$ denotes the specific entropy and k^0 denotes the conductivity tensor pulled back to the undeformed configuration according to

$$k^0 = \det(F) F^{-1} k F^{-T} \tag{6}$$

where k is the conductivity tensor in the deformed configuration.

To complete the formulation of the problem, it is necessary to define the material constitutive relations that stem from the Helmholtz free energy (per unit mass) $\mathcal{F}$, defined as

$$\mathcal{F} = \mathcal{E} - T\mathcal{S} \tag{7}$$

where $\mathcal{E}$ denotes the elastic energy. Specifically, one has

$$\rho_0 \left(\frac{\partial \mathcal{F}}{\partial E_{ij}}\right)_T = S_{ij} \tag{8}$$

and

$$\left(\frac{\partial \mathcal{F}}{\partial T}\right)_{E_{ij}} = -\mathcal{S} \tag{9}$$

where E denotes the Green strain tensor; that is,

$$E_{ij} = \tfrac{1}{2}(F_{ki} F_{kj} - \delta_{ij}) \tag{10}$$

In the present investigation, the Duhamel–Neumann form of the Helmholtz free energy [14] will be assumed; that is,

$$\rho_0 \mathcal{F} = \tfrac{1}{2} C_{ijkl} E_{ij} E_{kl} - C_{ijkl} \alpha_{kl}(T - T_0) E_{ij} + f(T, T_0) \tag{11}$$

where C denotes the fourth-order elasticity tensor, $\boldsymbol{\alpha}$ is the second-order tensor of thermal expansion, T_0 is the reference temperature, and [14]

$$f(T, T_0) = -\rho_0 C_v T_0 \left[\frac{T}{T_0} \ell_n \left(\frac{T}{T_0} \right) - \frac{T}{T_0} + 1 \right] \qquad (12)$$

in which C_v is the specific heat per unit mass measured in the state of constant strain.

Introducing Eqs. (11) and (12) in Eqs. (8) and (9) leads to the stress–strain relation

$$S_{ij} = \rho_0 \left(\frac{\partial \mathcal{F}}{\partial E_{ij}} \right)_T = C_{ijkl}[E_{kl} - \alpha_{kl}(T - T_0)] \qquad (13)$$

and to the rate of change of the specific entropy:

$$\dot{\mathcal{S}} = -\frac{\partial^2 \mathcal{F}}{\partial E_{ij} \partial T} \dot{E}_{ij} - \frac{\partial^2 \mathcal{F}}{\partial T^2} \dot{T} = \frac{1}{\rho_0}[C_{ijkl}\alpha_{kl}\dot{E}_{ij}] + \frac{C_v}{T}\dot{T} \qquad (14)$$

Combining Eqs. (5) and (14) finally yields the desired heat conduction equation:

$$\rho_0 C_v \frac{\partial T}{\partial t} - \frac{\partial}{\partial X_i}\left(k_{ij}^0 \frac{\partial T}{\partial X_j} \right) = -T C_{ijkl}\alpha_{kl}\frac{\partial E_{ij}}{\partial t} \qquad (15)$$

In the sequel, it will be useful to rewrite Eq. (15) as

$$\rho_0 C_v \frac{\partial T}{\partial t} - \frac{\partial}{\partial X_i}\left(k_{ij} \frac{\partial T}{\partial X_j} \right)$$
$$= -T C_{ijkl}\alpha_{kl}\frac{\partial E_{ij}}{\partial t} + \frac{\partial}{\partial X_i}\left[(k_{ij}^0 - k_{ij})\frac{\partial T}{\partial X_j} \right] \qquad (16)$$

in which $k_{ij} = k_{ij}[\boldsymbol{x}(\boldsymbol{X})]$ and the deformations dependent terms are lumped in the right-hand side. In the right-hand-side of Eq. (16), one recognizes the latency effect (the first term) and a change of geometry effect affecting the conductivity tensor (the second term). The specification of conditions on the boundary $\partial\Omega_0$ of the domain Ω_0 completes the formulation of the field equations.

The derivation of the governing equations for the generalized coordinates $q_n(t)$ and $\tau_n(t)$ is then achieved by introducing Eqs. (1) and (2) in (3), (4), (10), (13), and (16) and proceeding with a Galerkin approach. This process leads to the ROM equations

$$M_{ij}\ddot{q}_j + D_{ij}\dot{q}_j + K_{ij}^{(1)}q_j - K_{ijl}^{(\text{th})}q_j\tau_l + K_{ijl}^{(2)}q_jq_l + K_{ijlp}^{(3)}q_jq_lq_p$$
$$= F_i + F_{il}^{(\text{th})}\tau_l \qquad (17)$$

and

$$B_{ij}\dot{\tau}_j + \tilde{K}_{ij}\tau_j + K_{ijl}^{(\text{st})}\tau_j\dot{q}_l = P_i + R_{ij}\tau_j \qquad (18)$$

In Eq. (17), M_{ij}, D_{ij}, $K_{ij}^{(1)}$, $K_{ijl}^{(2)}$, and $K_{ijlp}^{(3)}$ denote the elements of the mass, damping, and linear stiffness matrices, and third- and fourth-order stiffness tensors associated with the quadratic and cubic terms. Furthermore, $K_{ijl}^{(\text{th})}$ and $F_i^{(\text{th})}$ are the change in the linear stiffness matrix and the force, both induced by a temperature variation of the form $1 \times T^{(m)}$. Finally, F_i denotes the ith modal force originating from the external excitation.

Although integral expressions for the preceding coefficients are obtained automatically as part of the Galerkin process (i.e., [17]; also see the Appendix), it has been found more convenient to evaluate them indirectly from the finite element model and some linear and nonlinear responses. For example, the evaluation of the stiffness coefficients $K_{ij}^{(1)}$, $K_{ijl}^{(2)}$, $K_{ijlp}^{(3)}$, and $K_{ijl}^{(\text{th})}$ can be achieved by the algorithm of [4] (see also [6,11,17]), which relies on an ensemble of nonlinear static solutions in which the displacements are prescribed and the necessary forces determined.

Furthermore, the terms $F_i^{(\text{th})}$ and F_i can conveniently be obtained from a finite element computation in which all degrees of freedom are blocked and in which either the temperature field (for $F_i^{(\text{th})}$) or the external loading (for F_i) is applied. Then, $F_i^{(\text{th})}$ and F_i are obtained as the projections on the basis function vector $\boldsymbol{U}_i^{(m)}$ of the reaction forces followed by a change of sign. Finally, the modal mass matrix is obtained as in the linear case; that is,

$$M_{ij} = \boldsymbol{U}^{(i)T}\boldsymbol{M}_{\text{FE}}\boldsymbol{U}^{(j)} \qquad (19)$$

where the superscript T designates the operation of matrix transposition. In Eq. (18), B_{ij} and $\tilde{K}_{ij}$ are the elements of the capacitance and conductance matrices of the ROM and are expressed in terms of their finite element counterparts as

$$B_{ij} = \boldsymbol{T}^{(i)T}\boldsymbol{B}_{\text{FE}}\boldsymbol{T}^{(j)}, \qquad \tilde{K}_{ij} = \boldsymbol{T}^{(i)T}\tilde{\boldsymbol{K}}_{\text{FE}}\boldsymbol{T}^{(j)} \qquad (20)$$

Furthermore, the term P_i denotes the source term associated with the boundary conditions, while R_{ij} corresponds to the projection on the basis function vector $\boldsymbol{T}^{(i)}$ of the last term on the right-hand side of Eq. (16). Integral expressions for all coefficients of Eq. (18) are given in the Appendix.

To complete the ROM strategy, it then remains to select the basis function vectors $\boldsymbol{U}_i^{(m)}$ and $\boldsymbol{T}^{(i)}$. Following the discussion of [11], the former were selected as the linear modes of the structure that would appear significantly in the linear response appended of an ensemble of dual modes that are obtained as specific nonlinear static solutions (see [11] for an extended presentation and validation in isothermal conditions).

In selecting basis functions for the thermal problem, $T^{(m)}(\boldsymbol{X})$, or their discretized, finite element counterparts $\boldsymbol{T}^{(i)}$, it was first recognized that the heat conduction is dominated by its through-thickness component. Accordingly, the functions $T^{(m)}(\boldsymbol{X})$ were split as

$$T^{(m)}(\boldsymbol{X}) = T_t^{(m)}(z)T_p^{(m)}(\boldsymbol{X}_p) \qquad (21)$$

where the first functions, $T_t^{(m)}(z)$, depended only on the through-thickness coordinate z, while the second ones, $T_p^{(m)}(\boldsymbol{X}_p)$, were functions of the remaining two coordinates combined in the vector $\boldsymbol{X}_p$. These latter functions could be divided into two classes: 1) functions $T_{p,\text{BC}}^{(m)}(\boldsymbol{X}_p)$, which were selected to satisfy the prescribed boundary conditions, and 2) functions $T_{p,\text{eig}}^{(m)}(\boldsymbol{X}_p)$, which were computed as the eigenvectors of the linear finite element approximation of the time-dependent heat conduction problem on the top and bottom surfaces (i.e., spanned by $\boldsymbol{X}_p$). The discretized counterpart of $T_{p,\text{eig}}^{(m)}(\boldsymbol{X}_p)$ thus satisfies an eigenvalue problem of the form

$$\tilde{\boldsymbol{K}}_{p,\text{FE}}\boldsymbol{T}_{p,\text{eig}}^{(m)} = \sigma_{p,m}\boldsymbol{B}_{p,\text{FE}}\boldsymbol{T}_{p,\text{eig}}^{(m)} \qquad (22)$$

Finally, the functions $T_t^{(m)}(z)$ were selected from the one-dimensional (1-D) heat conduction through the thickness, either as its steady solution or the eigenvectors of its time-dependent counterpart,

$$\tilde{\boldsymbol{K}}_{t,\text{FE}}\boldsymbol{T}_t^{(m)} = \sigma_{t,m}\boldsymbol{B}_{t,\text{FE}}\boldsymbol{T}_t^{(m)} \qquad (23)$$

or as linear combination of these functions.

The specific selection of these functions will be discussed in detail in the thermal ROM validation examples.

III. Validation Examples

The nonlinear ROM scheme previously described was assessed in this first validation effort on an isotropic flat beam and a FGM flat panel, both of which will be subjected to various thermal and acoustic loads.

Table 1 Clamped–clamped beam properties

Property	Value
Beam length	0.2286 m
Cross-sectional width	0.0127 m
Cross-sectional thickness	7.7510^{-4} m
Mass per unit length	7875 kg/m^3
Young's modulus	205,000 MPa
Shear modulus	80,000 MPa
Coeff thermal expansion	$2.510^{-5}/°C$

For the results presented and the materials considered, it was first observed that the effects of the deformations on the thermal problem, i.e., the latency effect [the third term in the left-hand side of Eq. (18)], and the change of geometry [the second term on the right-hand side of Eq. (18)] were small enough to be neglected. Thus, only a one-way coupling, the thermal problem influencing the structural one, was necessary.

The isotropic beam of properties given in Table 1 and its 40 CBEAM MSC.Nastran finite element model was considered first for the ROMs validation.

These validation efforts initially focused on the nonlinear structural ROM alone: i.e., with a fixed temperature distribution. Specifically, shown in Figs. 1 and 2 are the static deformations, transverse and in-plane, induced by applied uniform temperatures
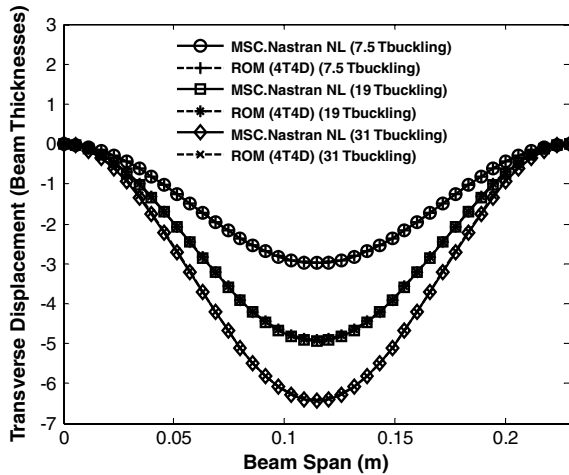
exceeding the buckling temperature, found by a SOL 105 to be 1.56°C. Note the excellent matching, at all temperatures, of the displacement fields obtained by a four-transverse–four-dual (4T4D) ROM and Nastran nonlinear (SOL 106). Given the symmetry of the beam and the temperature, only symmetric transverse motions and antisymmetric in-plane displacements were considered here as basis functions. Specifically, the first four symmetric linear modes of the unheated beam were considered for the transverse basis, while the four duals corresponding to the transverse mode 1 dominant were used. In addition, the proper orthogonal decomposition (POD)-based dual-mode construction procedure was performed for each mode, using 28 different loading factors (half positive and half negative) capable of producing peak deflections ranging from linear to approximately 4.34 beam thicknesses (see [11] for discussion).

A dynamic transverse loading was next added to the previous increases in temperatures. The corresponding distribution of forces was uniform along the beam but white with respect to time with energy in the band [0, 1042] Hz to simulate an acoustic loading. Such a loading will induce snap-throughs of the beam from one of its buckling positions to the other, with the frequency of these snap-through events dictated by the magnitude of the dynamic loading.

A detailed discussion of the panel response during these snap-throughs [12] has shown, in particular, that the symmetric loading will nevertheless induce an asymmetric response of the beam as it is snapping through the undeformed unheated configuration. That investigation has further demonstrated the capability of nonlinear ROMs based on linear transverse and in-plane modes to accurately capture the beam response during these highly nonlinear events.

Then, this first dynamic validation will provide a further assessment of the linear transverse-plus-dual mode basis for the prediction of the heated beam response. To capture the lack of symmetry, the previous ROM was enriched through the addition of the first antisymmetric mode and of the corresponding duals leading to a reduced model with five transverse and nine dual modes. In addition, the POD-based dual-mode construction procedure was performed for each mode, using 10 different loading factors (half positive and half negative) capable of producing peak deflections ranging from linear to approximately 1.2 beam thicknesses (see [11] for discussion). Furthermore, to permit a close comparison between the Nastran and ROM results, a simple Rayleigh damping model was adopted: that is, for which the damping matrix is $\boldsymbol{D} = \alpha \boldsymbol{M} + \beta \boldsymbol{K}$ with $\alpha = 12.838/s$ and $\beta = 2.061\mathrm{E}-6$ s. This selection leads to damping ratios between 0.5 and 1.3% for all five transverse modes in the excitation band.

Shown in Figs. 3–5 are the power spectra of the transverse displacement of the beam middle and the in-plane displacement at the beam quarter point corresponding to acoustic excitations of overall sound pressure levels, or simply sound pressure levels (SPLs), of 138, 148, and 168 dB, respectively, combined with a temperature increase of 12°C, or 7.5 times the buckling temperature. At the 138 dB loading, the response of the beam is around the buckling state with no snap-through observed within 12 s, as can be observed from the time history of the beam displacements (not shown here for brevity). At the intermediate loading case (148 dB see Fig. 4), the motion is mixed with periods of oscillations around the buckled states interrupted by snap-throughs. Finally, at the highest loading level (168 dB, see Fig. 5), the beam is seen from the time history to vibrate continuously from one buckled position to the other. Notwithstanding these differences in physics, the 14-mode ROM provides a very good to excellent matching of the finite element results in both transverse and in-plane directions and for all three cases.

In anticipation for the coupling of the thermal and structural problems, it was desired next to assess the nonlinear structural dynamic ROM in the presence of a more complex temperature distribution. To this end, the preceding analysis was repeated with a linear temperature distribution on the top surface, ranging from 25 to 75°C while the bottom surface was maintained at the reference temperature 0°C. In this loading scenario, the response is no longer expected to be symmetric, and thus the 4T4D-mode ROM had to be once again enriched. A different enrichment scheme was investigated

Fig. 1 Transverse deflections induced by panel temperature increases of 12, 30, and 50°C or 7.5, 19, and 31 T_{buckling}: ROM (4T4D) and nonlinear static finite element analysis (MSC.Nastran NL).
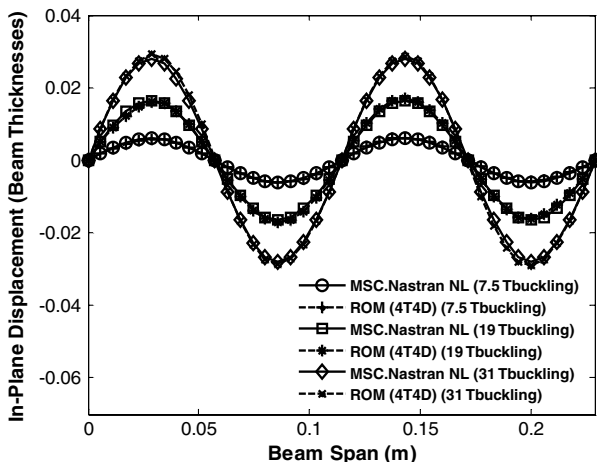

Fig. 2 In-plane deflections induced by panel temperature increases of 12, 30, and 50°C or 7.5, 19, and 31 T_{buckling}: ROM (4T4D) and nonlinear static finite element analysis (MSC.Nastran NL).
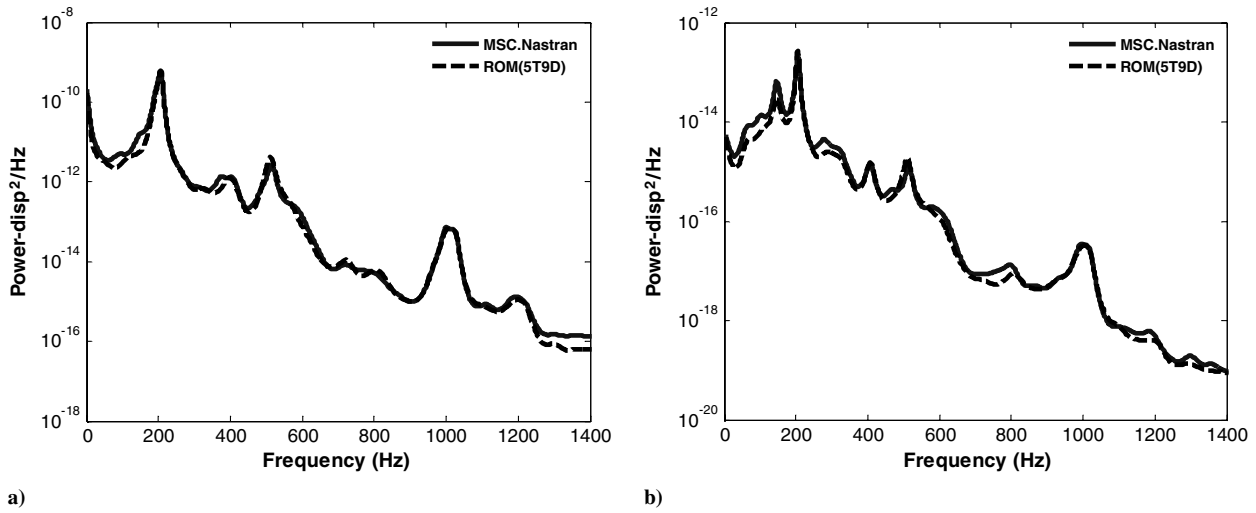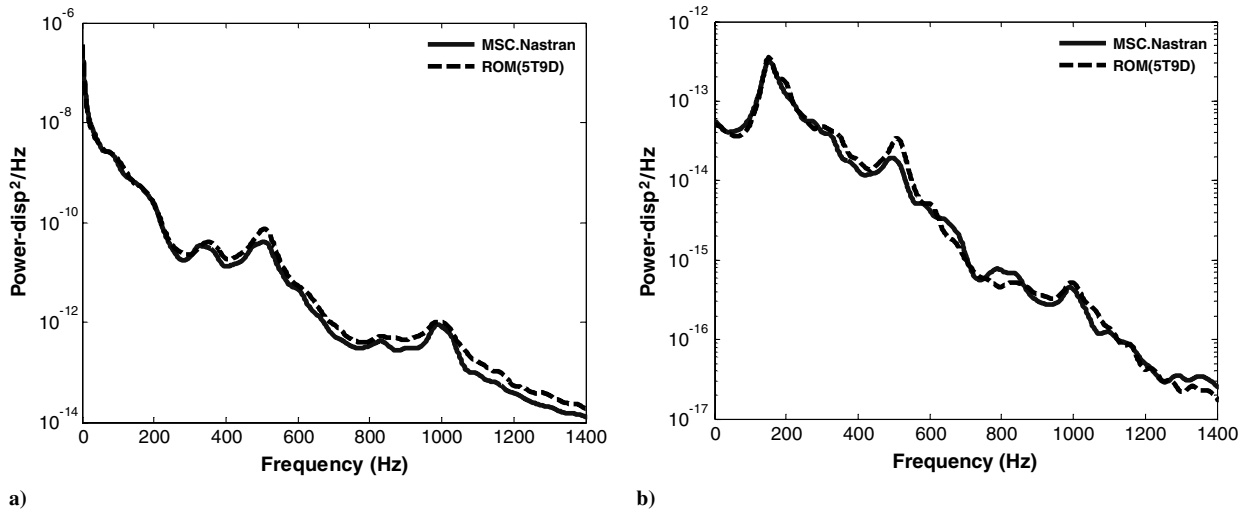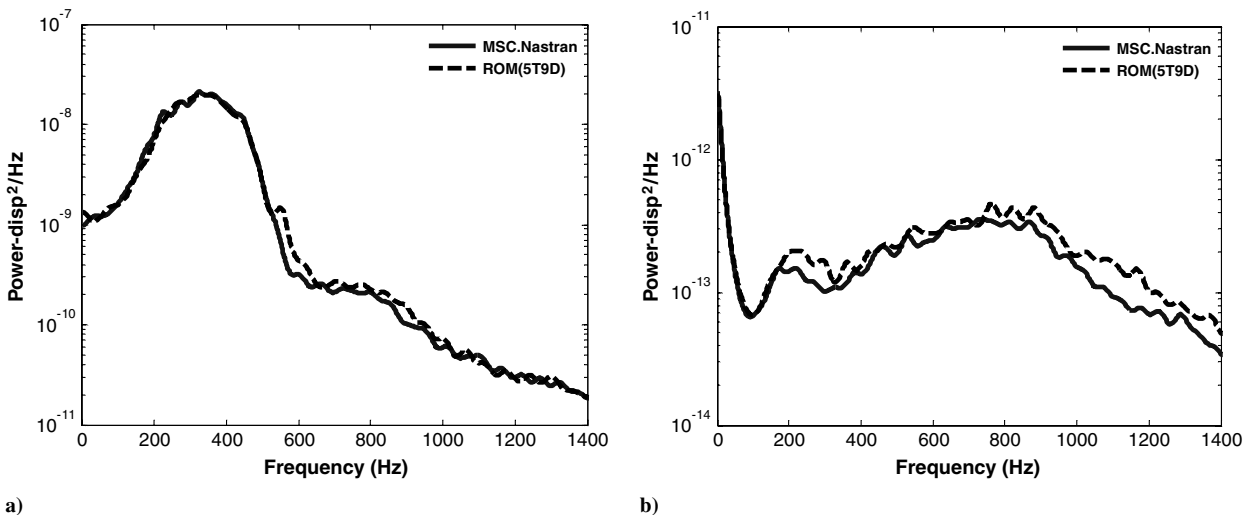
Fig. 3 Power spectral density of a) the transverse deflections of the beam middle and b) the in-plane displacement at the quarter point of the beam: ROM five transverse nine dual (5T9D) and finite element analysis (MSC.Nastran), SPL = 138 dB, and $\Delta T = 12°$C.

Fig. 4 Power spectral density of a) the transverse deflections of the beam middle and b) the in-plane displacement at the quarter point of the beam: ROM (5T9D) and finite element analysis (MSC.Nastran), SPL = 148 dB and $\Delta T = 12°$C.

Fig. 5 Power spectral density of a) the transverse deflections of the beam middle and b) the in-plane displacement at the quarter point of the beam: ROM (5T9D) and finite element analysis (MSC.Nastran), SPL = 168 dB and $\Delta T = 12°$C.
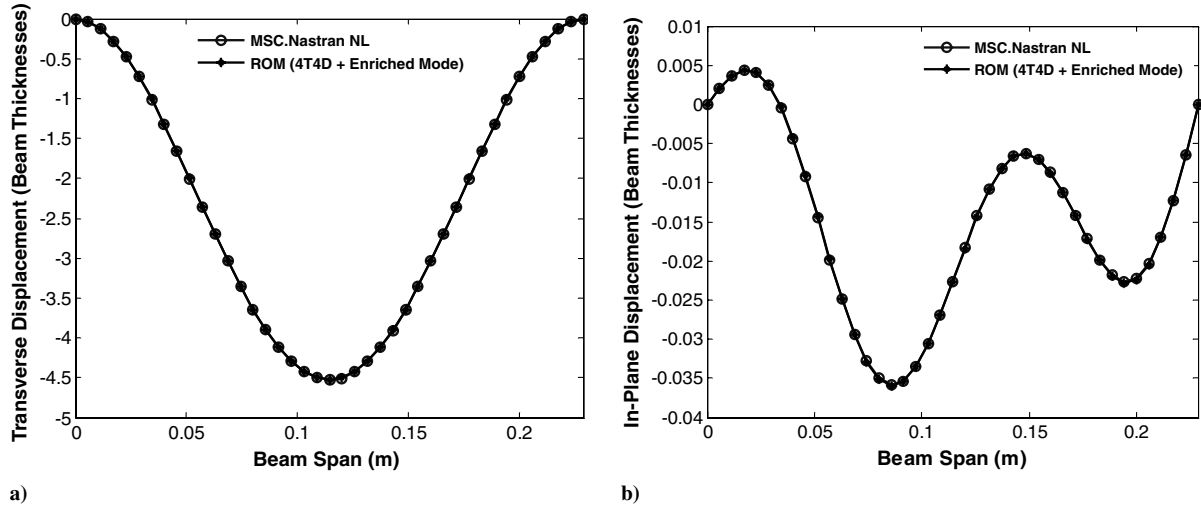
Fig. 6   Deflections induced by the temperature distribution in a) transverse and b) in-plane directions: enriched ROM (4T4D) and nonlinear finite element analysis (MSC.Nastran NL).

here, with the addition to the eight-mode model of the static nonlinear response of the beam to a linear temperature field, different in magnitude from the one applied. This surrogate temperature field was selected here as linear from 5 to 15°C, with the bottom surface maintained at the reference temperature of 0°C. The addition of the corresponding in-plane and transverse motions led to a nine-mode ROM. Furthermore, the POD-based dual-mode construction procedure was performed for each mode, using 10 different loading factors (half positive and half negative) capable of producing peak deflections ranging from linear to approximately 4.34 beam thicknesses (see [11] for discussion).

Shown in Fig. 6 are the transverse and in-plane displacements due to the applied temperature (at the top linear from 25 to 75°C, and 0°C at the bottom) acting alone. Furthermore, shown in Figs. 7 and 8 are power spectra of the transverse and in-plane responses due to acoustic excitations in the range of [0, 1042] Hz of SPLs of 143 and 168 dB, for which there is no snap-through and continuous snap-throughs, respectively. Again, a very good to excellent agreement is obtained in all cases.

The second phase of the validation process focused on the thermal ROM alone for the beam. Following the preceding discussion, the basis functions were selected in the form of Eq. (21). Since the present problem is steady, the functions $T_t^{(m)}(z)$ were selected as the solutions of the steady 1-D through thickness heat conduction problem; that is,

$$T_t^{(m)}(z) = z \qquad (24a)$$

and

$$T_t^{(m)}(z) = h - z \qquad (24b)$$

since the beam is isotropic. In Eqs. (24a) and (24b), z is the through-thickness coordinate vanishing at the lower surface and h is the thickness.

Next, the functions $T_p^{(m)}(X_p)$ were obtained from the 1-D heat conduction problem along the direction $X_p = x$ of the beam. Specifically, the functions $T_{p,\mathrm{eig}}^{(m)}(X_p)$ were selected as the eigenvectors of the time-dependent heat conduction problem with fixed temperatures at the left ($x = 0$) and right ($x = L$) ends of the beams. These functions were estimated from the eigenvector problem of Eq. (22) and here approximate sine functions. Since the temperature is assumed fixed at the two ends of the beam, all functions $T_{p,\mathrm{eig}}^{(m)}(X_p)$ vanish at both $x = 0$ and L. To induce the convergence of the expansion, it was thus necessary to add two functions $T_{p,\mathrm{BC}}^{(m)}(X_p)$ that match the boundary conditions at both $x = 0$ and L. This was achieved here by simply selecting $T_{p,\mathrm{BC}}^{(m)}(X_p)$ to be linear in x, and thus a linear combination of the functions x and $x - L$.
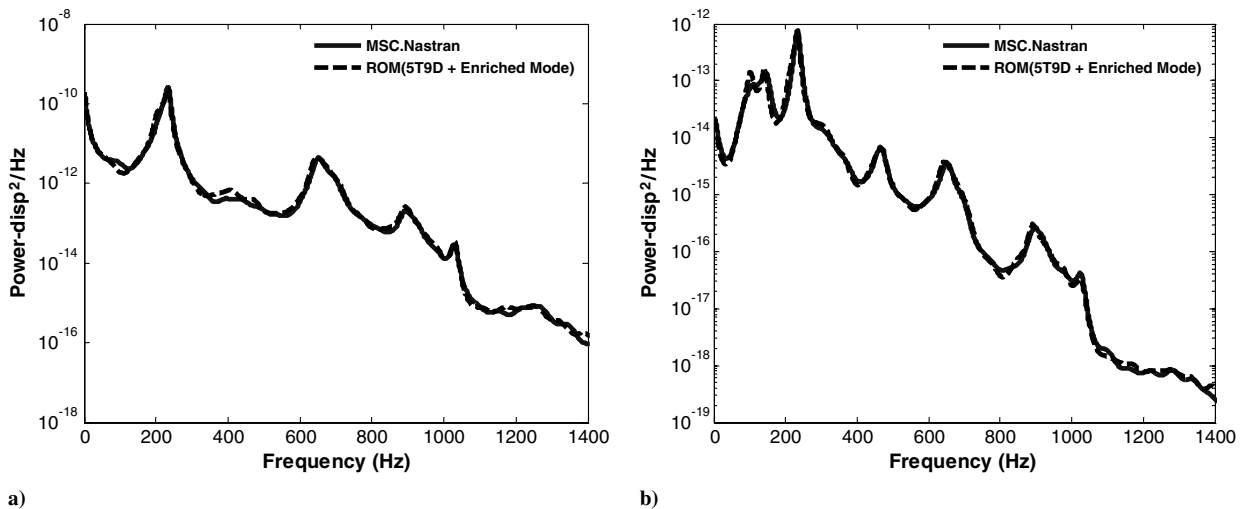

Fig. 7   Power spectral density of a) the transverse deflections of the heated beam middle and b) the in-plane displacement at the quarter point of the heated beam: enriched ROM (5T9D) and finite element analysis (MSC.Nastran); SPL = 143 dB.
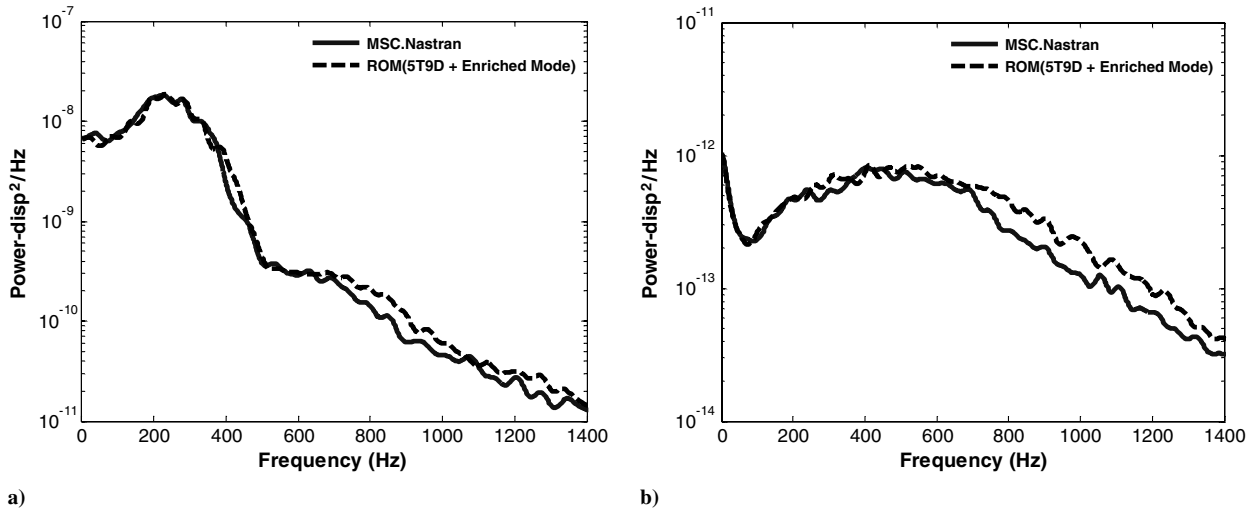
Fig. 8 Power spectral density of a) the transverse deflections of the heated beam middle and b) the in-plane displacement at the quarter point of the heated beam: enriched ROM (5T9D) and finite element analysis (MSC.Nastran); SPL = 168 dB.
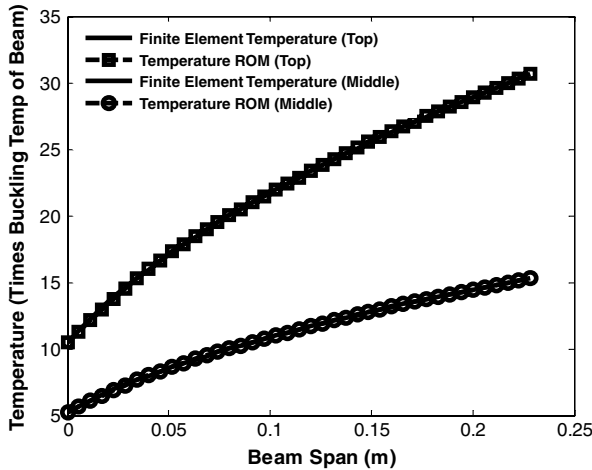

Fig. 9 Temperature distributions along the beam on the top surface and in the middle, scaled by the buckling temperature (1.6°C). Finite element results and ROM.
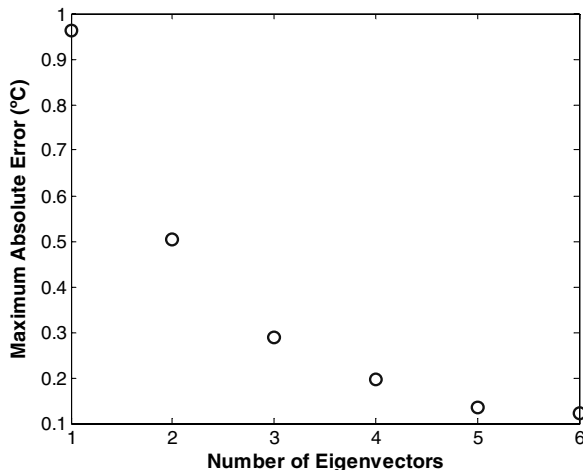

Fig. 10 Convergence of the thermal expansion as a function of the number of eigenvectors $T_{p,\mathrm{eig}}^{(m)}(X_p)$.

The convergence of the thermal expansion using the preceding basis functions was assessed by considering a temperature distribution in the form of a square root in the range of 18–50°C on the top with a zero temperature at the bottom (see Fig. 9).

As shown in Fig. 10, the convergence of the expansion is fast, and a maximum relative error of 1% (or 0.2°C as it occurs at the left side) is obtained with as few as four functions $T_{p,\mathrm{eig}}^{(m)}(X_p)$, to which must be added the two linear functions forming $T_{p,\mathrm{BC}}^{(m)}(X_p)$. The thermal ROM thus included six basis functions and matched the finite element results very well (see Fig. 9).

The first assessment of the combined thermal and structural ROM approach focused on the static response of the beam to the temperature distribution of Fig. 9. The reference computations were carried out with Nastran with the exact temperature distribution. The ROM predictions were, however, carried out with the six thermal basis functions, and to each one of those corresponded a linear stiffness matrix $K_{ijl}^{(\mathrm{th})}$ [in Eq. (17)].

The structural basis selected consisted of the 4T4D modes developed before with the single-mode enrichment corresponding to the nonlinear response to linear temperatures of 5–25°C on the top and zero on the bottom (as for Figs. 6–8). In addition, the POD-based dual-mode construction procedure was performed for each mode, using 10 different loading factors (half positive and half negative) and capable of producing peak deflections ranging from linear to approximately 1.2 beam thicknesses (see [11] for discussion).

Shown in Fig. 11 are the transverse and in-plane displacements obtained by Nastran and by the ROM. Clearly, the matching is excellent.

The next assessment task was focused on both the temperature distribution of Fig. 9 and a transverse excitation inducing significant snap-throughs. To this end, shown in Fig. 12 are power spectra of the transverse and in-plane deflections due to an acoustic excitation of SPL of 168 dB, as predicted by Nastran and by a ROM involving both of the enrichment investigated in earlier cases. That is, the structural ROM was formed with the first four symmetric transverse modes, the first antisymmetric transverse mode, nine duals based on the first symmetric and antisymmetric modes as dominant, and the static nonlinear response to linear temperatures of 5 to 15°C on the top and zero on the bottom. Again, a very good to excellent agreement is obtained throughout the frequency range of excitation. In addition, the POD-based dual-mode construction procedure was performed for each mode, using the same loading factors as for the static validation results.

The final phase of the present validation effort focused on the FGM clamped plate considered in [11]. In this past investigation, it was
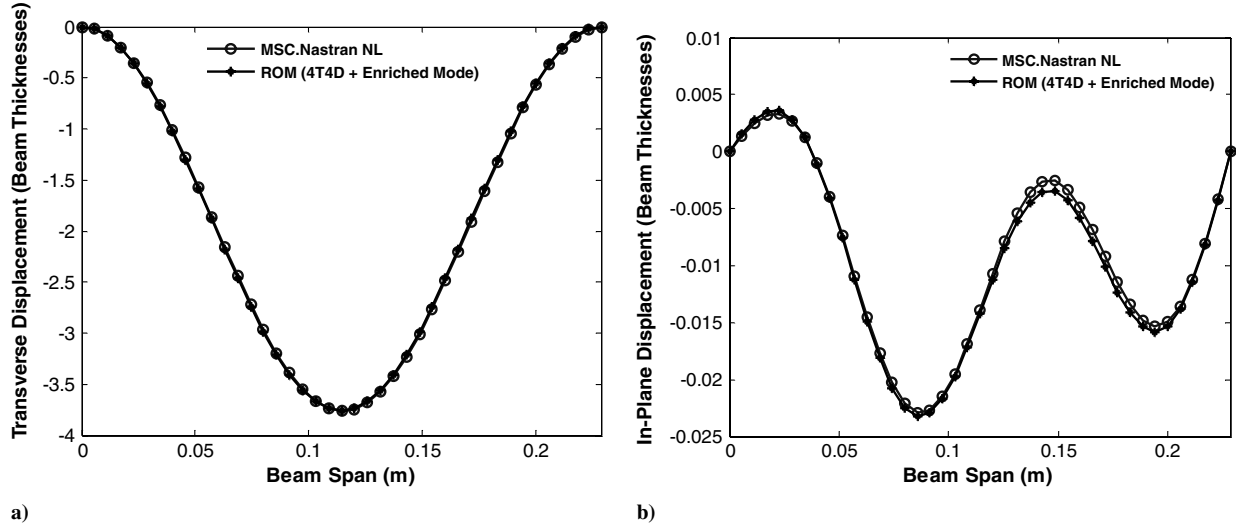
Fig. 11   Deflections induced by the square-root temperature distribution in a) transverse and b) in-plane directions: enriched ROM (4T4D) and nonlinear finite element analysis (MSC.Nastran NL).
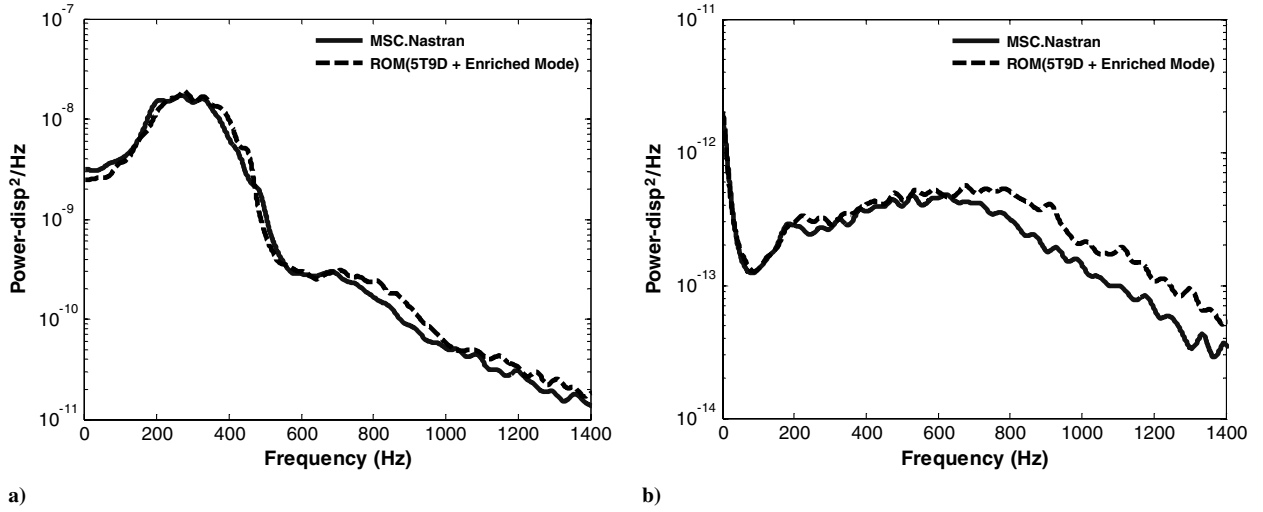

Fig. 12   Power spectral density of a) the transverse deflections of the heated beam middle and b) the in-plane displacement at the quarter point of the heated beam: enriched ROM (5T9D) and finite element analysis (MSC.Nastran); SPL = 168 dB.
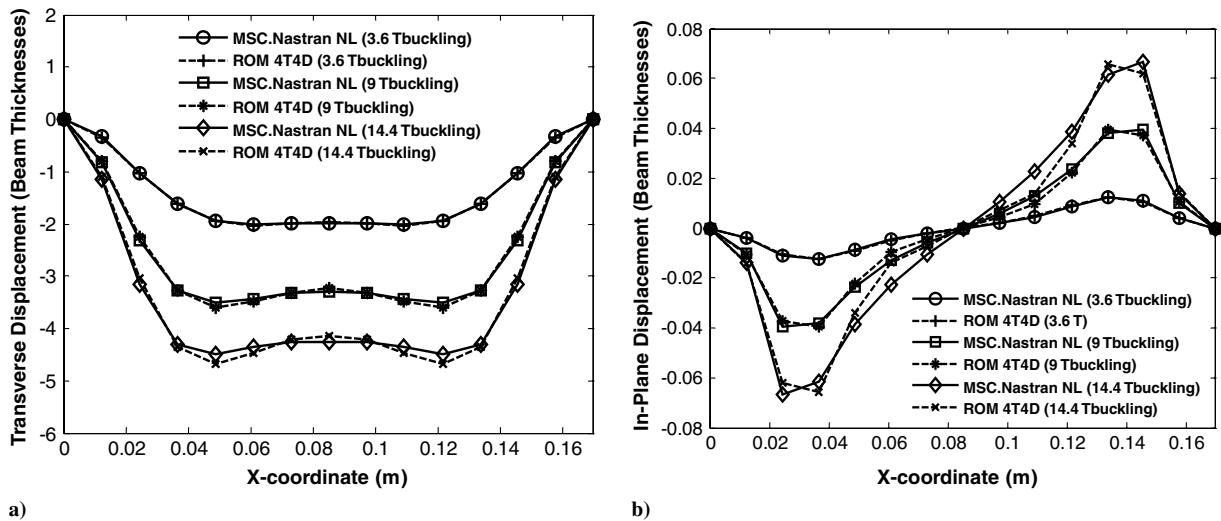

Fig. 13   Deflections induced by panel temperature increases of 20, 50, and 80°C, or 3.6, 9, and 14.4 T_{buckling}, along the X axis at $Y = 0.0475$ m (middle) a) transverse and b) in-plane X directions: ROM (4T4D) and nonlinear static finite element analysis (MSC.Nastran NL).

shown that the isothermal response of the panel to transverse acoustic loads could be very well predicted with a ROM composed of five symmetric transverse modes and the five duals with mode 1 dominant. Furthermore, the POD-based dual-mode construction procedure was performed for each mode, using 22 different loading factors (half positive and half negative) inducing deflections ranging from linear to a 1.2 plate thickness. In this light, it is desired here to extend this work and assess the capability of ROMs to predict the thermoelastic response of this FGM plate, which is composed of 20% SiC (on the top of the panel) and 80% aluminum (on the bottom of the panel). The panel dimensions were 0.17 m (along X) $\times$ 0.095 m (along Y) $\times 5E - 4$ m total thickness (along Z), and they were discretized using 14×10 CQUAD4 elements.

The first assessment of ROMs on this FGM panel focused on the prediction of the buckled shape due to uniform increases of temperature. Shown in Fig. 13 are the transverse and in-plane displacements obtained by Nastran and a 4T4D ROM for rises in temperature of 20, 50, and 80°C or, equivalently, of 3.6, 9, and 14.4 times the buckling temperature estimated from Nastran SOL 105 as 5.6°C. Again, an excellent matching is observed.

The prediction of the dynamic response, including snap-throughs, of the heated panel subjected to an additional acoustic excitation was achieved next. Specifically, shown in Fig. 14a are the power spectra of the transverse displacement induced at the panel middle by an acoustic excitation white in the band [0, 2780 Hz]. Furthermore, the SPL is 143 dB and is such that the panel does not exhibit any snap-through within the 9 s of computations. Continuous snap-throughs do not occur for this panel until approximately 178 dB. A 20-mode model built with seven transverse and 13 dual modes was adopted that provides an excellent matching of the Nastran transverse response (see Fig. 14a). Furthermore, the POD-based dual-mode construction procedure was performed for each mode, using the same 22 loading factors as in the static validation. In regard to in-plane displacements, it was decided to compare the Nastran and ROM predictions at the points where these displacements (i.e., their variance) are largest. For the displacement along the long side X, this maximum takes place at point A of coordinates (0.049, 0.0475) m. For the displacement along the short side Y, it is at B: (0.085, 0.0285) m. Accordingly, shown in Figs. 14b and 14c are the power spectra of the displacements along x at A and along y at B. Again, an excellent match of the Nastran results is obtained.

Previously, it was stated that continuous snap-throughs do not occur until approximately 178 dB for a panel temperature of 20°C. Such a large excitation leads to a very rich response as the panel goes from one buckled configuration to the other. Thus, a large basis would be necessary to properly capture the ensuing motion. However, it was desired to show that the ROM strategy is still capable of accurately capturing the response of the FGM panel in the intermittent and continuous snap-through cases without developing such a large model. To this end, the temperature of the panel was decreased from 20 to 8°C, or approximately $1.4T_{\text{buckling}}$. The acoustic excitation was once again modeled as white noise in the band [0,2780] Hz. Furthermore, a SPL of 141 dB was used to induce a motion with intermittent snap-throughs, and a SPL of 151 dB was used to create a continuous snap-through response. A 19-mode model, built with 10 transverse and nine dual modes, was adopted. In addition, the POD-based dual-mode construction procedure was performed for each mode, using 24 different loading factors (half positive and half negative) resulting in peak deflections ranging from linear to a 1.5 plate thickness. Shown in Figs. 15 and 16 are the power spectra of the transverse displacement at the panel middle point, the in-plane displacement along the long side X at point A, and the in-plane displacement along the short side Y at point B, where the location of points A and B was defined in the previous discussion. Clearly, an excellent match of the Nastran results was again achieved.

The final validation effort focused on the thermal ROM and, more specifically, on the assessment of its convergence. To this end, the top of the panel was subjected to a square-root temperature profile from 400 to 475°C along the long side (no temperature variation in y),
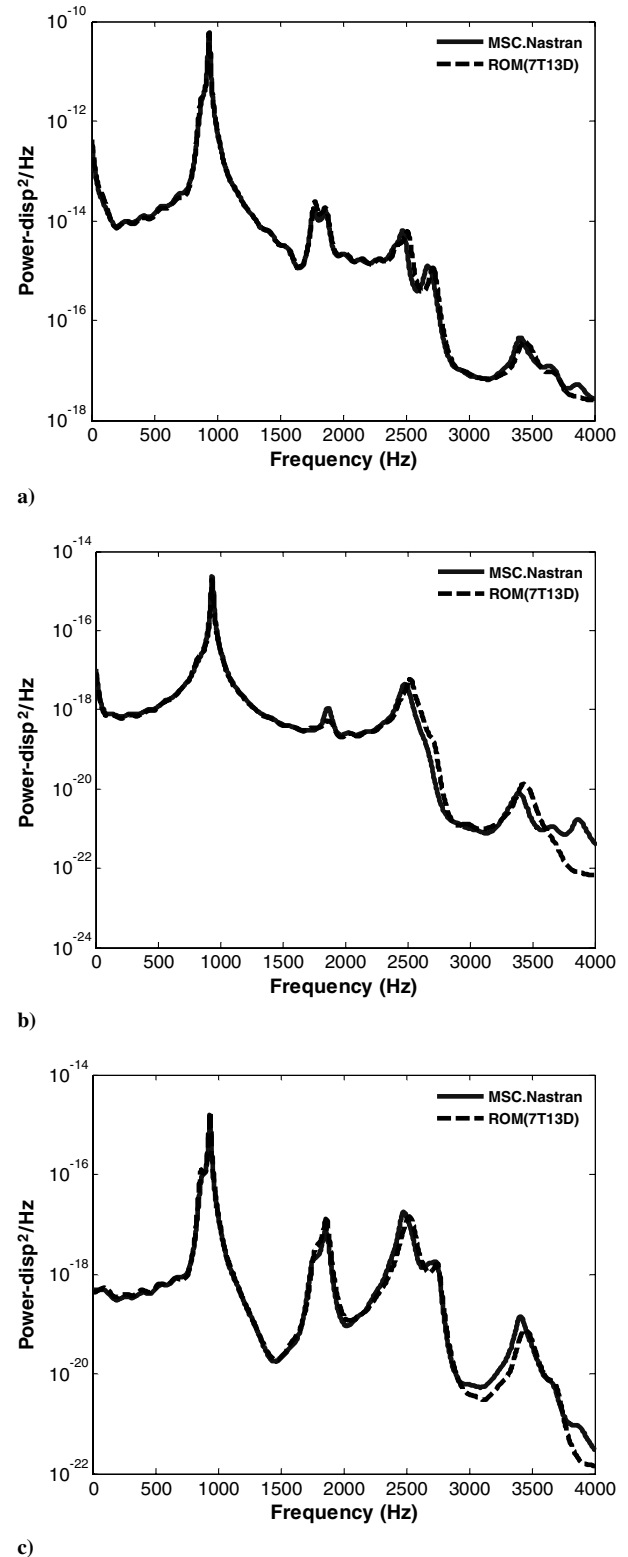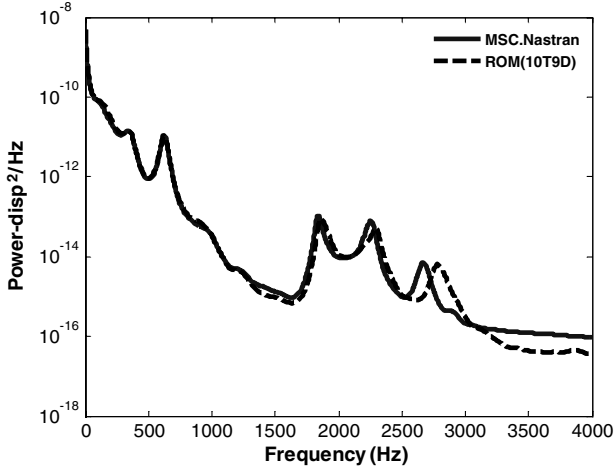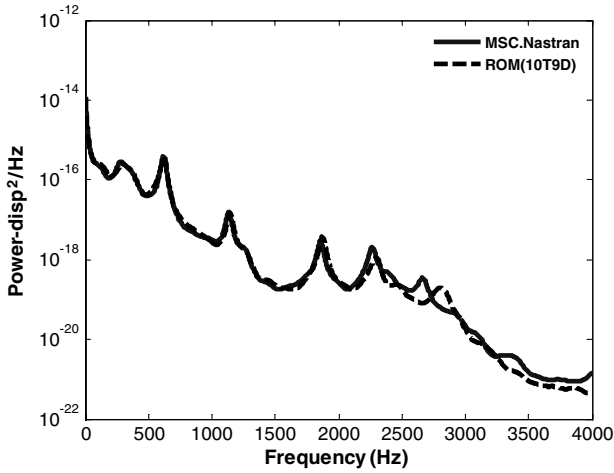

a)

b)

c)

Fig. 14 Power spectral density of the response of the FGM panel heated at 20°C: a) transverse deflections at the middle, b) in-plane displacement along the long side at point A, and c) in-plane displacement along the short side at point B. ROM seven transverse 13 dual (7T13D) and finite element analysis (MSC.Nastran); SPL = 143 dB.

while the bottom was maintained at the reference temperature of 0°C. The thermal basis was selected as before except for the function $T_t^{(m)}(z)$, which exhibited a bilinear form owing to the difference in the thermal properties of the SiC and aluminum.
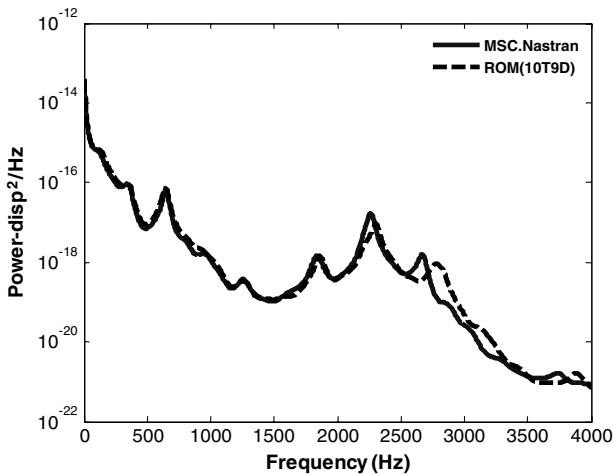
As seen in Fig. 17, the thermal ROM converged quickly, and a model with four eigenvectors and two functions $T_{p,\text{BC}}^{(m)}(X_p)$ (i.e., six
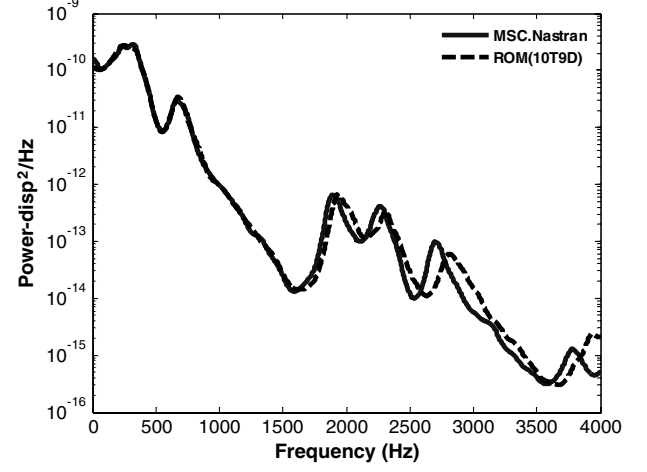
a)

b)

c)

Fig. 15 Power spectral density of the response of the FGM panel heated at 8°C: a) transverse deflections at the middle, b) in-plane displacement along the long side at point A, and c) in-plane displacement along the short side at point B. ROM (10T9D) and finite element analysis (MSC.Nastran); SPL = 141 dB.
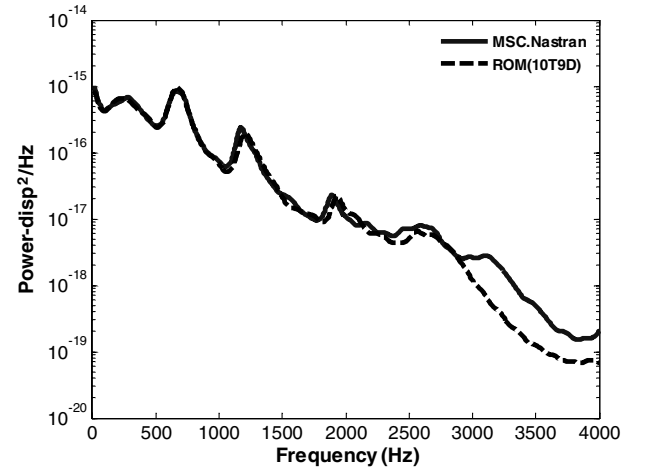

a)

b)

c)

Fig. 16 Power spectral density of the response of the FGM panel heated at 8°C: a) transverse deflections at the middle, b) in-plane displacement along the long side at point A, and c) in-plane displacement along the short side at point B. ROM (10T9D) and finite element analysis (MSC.Nastran); SPL = 151 dB.
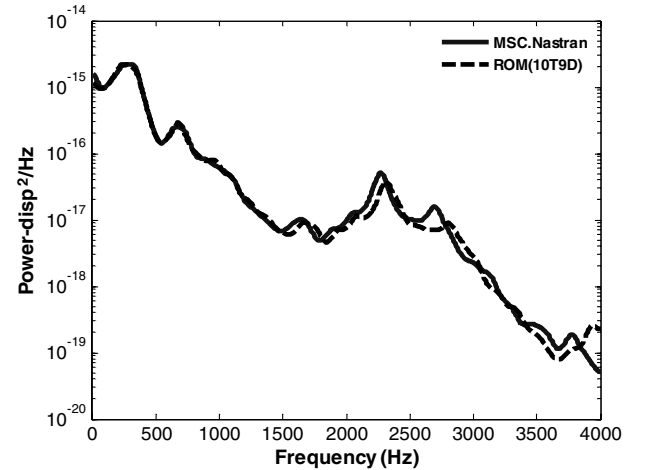
basis functions) was retained. This model provides an excellent match of the prescribed temperature at the top surface and the finite element predicted temperature at the middle, as seen in Fig. 18. In fact, the maximum absolute error is only 0.3°C, or less than 0.1%.

IV. Computational Times

Having demonstrated the accuracy of the ROM approach in the previous section, it is now appropriate to highlight one of its advantages over full finite element analyses: namely, the significant reduction in computational effort/time. A complete and precise
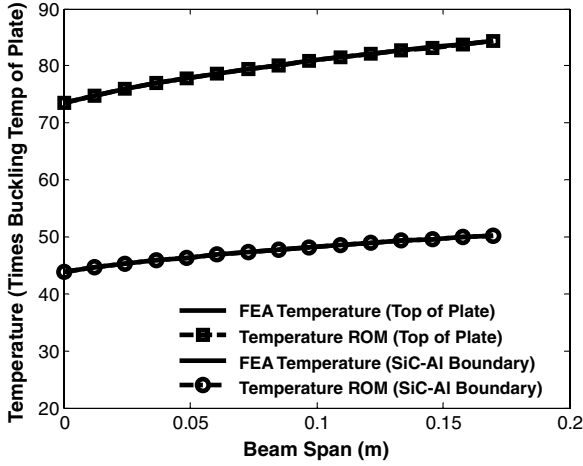
Fig. 17 Temperature distributions along the long side on the panel top surface and in the middle, scaled by the buckling temperature (5.6°C): finite element analysis (FEA) and ROM.
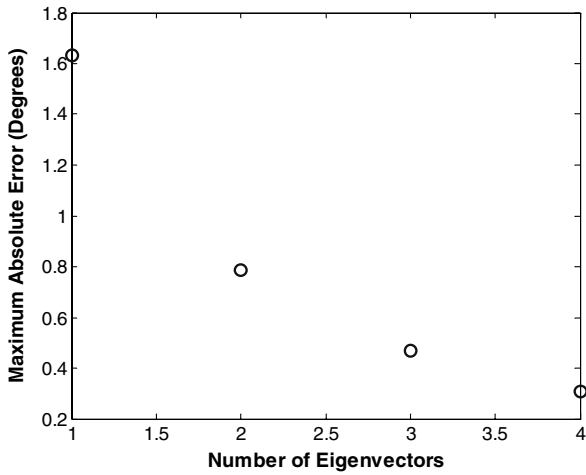

Fig. 18 Convergence of the thermal expansion as a function of the number of eigenvectors $T_{p,\mathrm{eig}}^{(m)}(X_p)$.

comparison of the computational efforts is difficult to achieve, as the two methods involve very different parameters: e.g., number of modes in the ROM vs number of nodes/degrees of freedom in the full model. Furthermore, Nastran is a commercial software that has been optimized, while the ROM solution was determined using an in-house code, which was written carefully but cannot be considered optimized. Nevertheless, a clarifying perspective on this issue was obtained here using the clamped–clamped beam model investigated in the previous section, considered without temperature under an acoustic loading corresponding to a SPL of 110 dB. The wall-clock times on the same computer needed for the Nastran and ROM computations are shown in Table 2 for an equal number of time steps. The tolerances on the solutions (all relative) were set, as in all computations in the previous section, to 10^{-9} on position for the ROM solutions and 10^{-6} on position and 10^{-5} on force balance in the Nastran ones.

Table 2 Run times (wall clock) of Nastran and ROM computations (in seconds)

Computations	Run time
MSC Nastran	2700
ROM (3 transverse–3 duals, 6 modes)	30–40
ROM (4 transverse–4 duals, 8 modes)	73
ROM (7 transverse–7 duals, 14 modes)	488

It is concluded from Table 2 that the ROM computations are indeed significantly faster, even using a noncommercial code, owing to the much reduced number of differential equations involved. However, it should be recognized that this reduced computational cost is not the only advantage of ROMs; they also significantly simplify coupled multidisciplinary analyses, as demonstrated here with heat conduction and in [13] with aerodynamics.

V. Conclusions

The focus of this investigation was on the development and validation of thermoelastic ROMs for the geometrically nonlinear response and temperature of heated structures. The proposed ROM approach is based on a modal-type expansion of both displacements and temperatures in the undeformed, unheated configuration. The governing equations for the generalized coordinates of both temperature and displacement fields were obtained from finite thermoelasticity through a Galerkin approach. The selection of the basis functions to be used in these ROMs was discussed, and the numerical evaluation of the model coefficients assessed.

A detailed validation effort was conducted on two different structural models, an isotropic beam and a FGM panel, both of which were subjected to a wide range of thermal effects and external loads. Owing to the small feedback of the structural deformations on the temperature field for the cases considered, the present validation effort was limited to the case of a temperature field uncoupled from the displacements, although the formulation developed does include latency and deformation effects. In all cases considered, the temperatures and displacements predicted by the ROMs were found to be in excellent agreement with those obtained with full finite element models.

Appendix

Proceeding with the Galerkin approximation of the finite thermoelasticity equations leads to Eqs. (17) and (18) with

$$M_{mn} = \int_{\Omega_0} \rho_0 U_i^{(m)} U_i^{(n)} \, d\boldsymbol{X} \tag{A1}$$

$$K_{mn}^{(1)} = \int_{\Omega_0} \frac{\partial U_i^{(m)}}{\partial X_k} C_{iklp} \frac{\partial U_l^{(n)}}{\partial X_p} \, d\boldsymbol{X} \tag{A2}$$

$$K_{mnp}^{(\mathrm{th})} = \int_{\Omega_0} \frac{\partial U_i^{(m)}}{\partial X_k} \frac{\partial U_i^{(n)}}{\partial X_j} C_{jklr} \alpha_{lr} T^{(p)} \, d\boldsymbol{X} \tag{A3}$$

$$K_{mnp}^{(2)} = \tfrac{1}{2}[\hat{K}_{mnp}^{(2)} + \hat{K}_{pmn}^{(2)} + \hat{K}_{npm}^{(2)}] \tag{A4}$$

$$\hat{K}_{mnp}^{(2)} = \int_{\Omega_0} \frac{\partial U_i^{(m)}}{\partial X_j} C_{ijkl} \frac{\partial U_r^{(n)}}{\partial X_k} \frac{\partial U_r^{(p)}}{\partial X_l} \, d\boldsymbol{X} \tag{A5}$$

$$K_{msnp}^{(3)} = \frac{1}{2} \int_{\Omega_0} \frac{\partial U_i^{(m)}}{\partial X_j} \frac{\partial U_i^{(s)}}{\partial X_k} C_{jklw} \frac{\partial U_r^{(n)}}{\partial X_l} \frac{\partial U_r^{(p)}}{\partial X_w} \, d\boldsymbol{X} \tag{A6}$$

$$F_m = \int_{\Omega_0} \rho_0 U_i^{(m)} b_i^0 \, d\boldsymbol{X} + \int_{\partial\Omega_0} U_i^{(m)} t_i^0 \, ds \tag{A7}$$

and

$$F_{mn}^{(\mathrm{th})} = \int_{\Omega_0} \frac{\partial U_i^{(m)}}{\partial X_k} C_{iklr} \alpha_{lr} T^{(n)} \, d\boldsymbol{X} \tag{A8}$$

for the coefficients of the structural dynamic ROM.

For the thermal ROM [Eq. (18)], one has

$$B_{mn} = \int_{\Omega_0} \rho_0 C_v T^{(m)} T^{(n)} \, d\boldsymbol{X} \tag{A9}$$

$$\tilde{K}_{mn} = \int_{\Omega_0} \frac{\partial T^{(m)}}{\partial X_i} k_{ij} \frac{\partial T^{(n)}}{\partial X_j} \, d\boldsymbol{X} \tag{A10}$$

$$K_{mnp}^{(st)} = \int_{\Omega_0} T^{(m)} T^{(n)} C_{ijkl} \alpha_{kl} \frac{\partial U_i^{(p)}}{\partial X_j} \, d\boldsymbol{X} \tag{A11}$$

$$P_m = \int_{\partial\Omega_0} T^{(m)} k_{ij} \tau_n \frac{\partial T^{(n)}}{\partial X_j} n_i \, ds \tag{A12}$$

$$R_{mn} = -\left[\iint_{\Omega_0} T^{(m)} T^{(n)} C_{ijkl} \alpha_{kl} \frac{\partial U_k^{(r)}}{\partial X_i} \frac{\partial U_k^{(s)}}{\partial X_j} \, d\boldsymbol{X} \right] q_r \dot{q}_s$$
$$+ \int_{\partial\Omega_0} T^{(m)} (k_{ij}^0 - k_{ij}) \frac{\partial T^{(n)}}{\partial X_j} n_i \, ds$$
$$- \int_{\Omega_0} \frac{\partial T^{(m)}}{\partial X_i} (k_{ij}^0 - k_{ij}) \frac{\partial T^{(n)}}{\partial X_j} \, d\boldsymbol{X} \tag{A13}$$

Acknowledgment

References

[1] Blevins, R. D., Holehouse, I., and Wentz, K. R., "Thermoacoustic Loads and Fatigue of Hypersonic Vehicle Skin Panels," *Journal of Aircraft*, Vol. 30, No. 6, 1993, pp. 971–978.
doi:10.2514/3.46441

[2] Weiting, A. R., Dechaumphai, P., Bey, K. S., Thornton, E., and Morgan, K., "Application of Integrated Fluid-Thermal-Structure Analysis Methods," *Thin-Walled Structures*, Vol. 11, Nos. 1–2, 1991, pp. 1–23.
doi:10.1016/0263-8231(91)90008-7

[3] McEwan, M. I., Wright, J. R., Cooper, J. E., and Leung, A. Y. T., "A Combined Modal/Finite Element Analysis Technique for the Dynamic Response of a Nonlinear Beam to Harmonic Excitation," *Journal of Sound and Vibration*, Vol. 243, No. 4, 2001, pp. 601–624.
doi:10.1006/jsvi.2000.3434

[4] Muravyov, A. A., and Rizzi, S. A., "Determination of Nonlinear Stiffness with Application to Random Vibration of Geometrically Nonlinear Structures," *Computers and Structures*, Vol. 81, No. 15, 2003, pp. 1513–1523.
doi:10.1016/S0045-7949(03)00145-7

[5] Hollkamp, J. J., Gordon, R. W., and Spottswood, S. M., "Nonlinear Modal Models for Sonic Fatigue Response Prediction: A Comparison of Methods," *Journal of Sound and Vibration*, Vol. 284, Nos. 3–5, 2005, pp. 1145–1163.
doi:10.1016/j.jsv.2004.08.036

[6] Mignolet, M. P., Radu, A. G., and Gao, X., "Validation of Reduced Order Modeling for the Prediction of the Response and Fatigue Life of Panels Subjected to Thermo-Acoustic Effects," *Proceedings of the 8th International Conference on Recent Advances in Structural Dynamics*, Southampton, U.K., 14–16 July 2003.

[7] Radu, A., Yang, B., Kim, K., and Mignolet, M. P., "Prediction of the Dynamic Response and Fatigue Life of Panels Subjected to Thermo-Acoustic Loading," 45th Structures, Structural Dynamics, and Materials Conference, Palm Springs, CA, AIAA Paper 2004-1557, April 2004.

[8] Przekop, A., and Rizzi, S. A., "Nonlinear Reduced Order Random Response Analysis of Structures with Shallow Curvature," *AIAA Journal*, Vol. 44, No. 8, 2006, pp. 1767–1778.
doi:10.2514/1.18868

[9] Gordon, R. W., and Hollkamp, J. J., "Reduced-Order Modeling of the Random Response of Curved Beams using Implicit Condensation," AIAA Paper 2006-1926, 2006.

[10] Spottswood, S. M., Hollkamp, J. J., and Eason, T. G., "Reduced-Order Models for a Shallow Curved Beam Under Combined Loading," *AIAA Journal* Vol. 48, No. 1, 2009, pp. 47–55.
doi:10.2514/1.38707

[11] Kim, K., Wang, X. Q., and Mignolet, M. P., "Nonlinear Reduced Order Modeling of Functionally Graded Plates," 49th Structures, Structural Dynamics, and Materials Conference, Schaumburg, IL, AIAA Paper 2008-1873, April 2008.

[12] Przekop, A., and Rizzi, S. A., "Dynamic Snap-Through of Thin-Walled Structures by a Reduced-Order Method," *AIAA Journal*, Vol. 45, No. 10, 2007, pp. 2510–2519.
doi:10.2514/1.26351

[13] Kim, K., Kim, Y. C., Mignolet, M. P., Liu, D. D., Chen, P. C., and Lee, D. H., "Random Aeroelastic Response Due to Strong Hypersonic Unsteady-Wave/Shock Interaction with Acoustic Loads," 48th Structures, Structural Dynamics, and Materials Conference, Honolulu, AIAA Paper 2007-2014, April 2007.

[14] Fung, Y. C., and Tong, P., *Classical and Computational Solid Mechanics*, World Scientific, River Edge, NJ, 2001.

[15] Bonet, J., and Wood, R. D., *Nonlinear Continuum Mechanics for Finite Element Analysis*, Cambridge Univ. Press, Cambridge, England, U.K., 1997.

[16] Vujosevic, L., and Lubarda, V. A., "Finite-Strain Thermoelasticity Based on Multiplicative Decomposition of Deformation Gradient," *Theoretical and Applied Mechanics*, Vols. 28–29, 2002, pp. 379–399.

[17] Mignolet, M. P., and Soize, C., "Stochastic Reduced Order Models for Uncertain Geometrically Nonlinear Dynamical Systems," *Computer Methods in Applied Mechanics and Engineering*, Vol. 197, Nos. 45–48, 2008, pp. 3951–3963.
doi:10.1016/j.cma.2008.03.032

A. Palazotto
Associate Editor